An Envelope Detection based Broadband Ultrasonic Ranging System for Improved Indoor/Outdoor Positioning

Prasant Misra[1] Sanjay Jha[1] Diet Ostry[2] Navinda Kottege[2]

[1] University of New South Wales, Australia
{pkmisra,sanjay}@cse.unsw.edu.au
[2] CSIRO, Australia
{Diet.Ostry, Navinda.Kottege}@csiro.au

Technical Report
UNSW-CSE-TR-1106
June 2011

THE UNIVERSITY OF
NEW SOUTH WALES

School of Computer Science and Engineering
The University of New South Wales
Sydney 2052, Australia

Abstract

Fine-grained location information at long range can benefit many applications of embedded sensor networks and robotics. In this paper, we focus on range estimation - an important prerequisite for fine-grained localization - in the ultrasonic domain for both indoor and outdoor environments, and make three contributions. First, we evaluate the characteristics of broadband signals, and provide useful statistics in their design and engineering to achieve a good trade-off between range and accuracy. Second, to overcome the inaccuracies due to correlation sidelobes, we propose a signal detection technique that estimates the envelope of the correlated pulse using a simple least-square approximation approach, and undertake a simulation study to verify its ranging efficiency on linear chirps. Third, leveraging on the insights obtained from our initial study, we present the design and implementation of two different ultrasonic broadband ranging systems based on linear chirps: (1): PC-based system using the most basic commodity hardware and custom designed units, and (2): Mote-based system using the CSIRO Audio nodes, which comprises of a Fleck-3z mote along with audio codecs and a Blackfin DSP. Our evaluation results for both the systems indicate that they are precise enough to support source localization applications: a reliable operational range of 45m and 20m (outdoor) respectively, and an average accuracy of approximately 2cm.

1 Introduction

A general acoustic source localization problem involves locating the sound source using acoustic sensors. It has many military and scientific applications, which include, tracking the movement of vehicles and personnel [1, 2], battlefield surveillance [3], population measurement of various species [4], environmental [5, 6] and habitat monitoring [7]. The reliability of the target location information is directly dependent on the accuracy of the position knowledge of the sensing node, where a minor estimation bias can result in localization errors that scale with range to the target. Sensing entities, with the knowledge of their precise location, can provision themselves as a positioning infrastructure to provide navigational support to robots and autonomous vehicles, enable automatic system calibration and collaborative sensing, provide valuable assistance in identification of micro-climate zones in precision agriculture, and facilitate search/rescue operations.

Despite significant progress in the related areas of location sensing systems, many of these outdoor systems operate in the acoustic (i.e. audible) range [8, 9, 10, 11, 12, 13], and therefore, may not suitable for a general ranging and localization strategy, especially for covert operations. Working in the ultrasonic domain provides the advantage of inconspicuous location sensing, but its applications have been restricted to only indoor environments that support dense deployment and require short coverage range [14, 15, 16]. There are various challenges using ultrasound as a physical layer technology. It is reported to be more sensitive to atmospheric absorption than acoustic signals, which may lead to a reduced coverage range. There are less available commercial off-the-shelf (COTS) components for ultrasonics, which increases the implementation timeline of potential applications. Besides, there are other very important factors limiting sound performance, such as reflections (from the environment, ground etc.), variation in air density caused by thermal effects leading to variation in sound speed, and also, propagation effects caused by non-uniformities in the atmosphere (due to wind and turbulence).

Detection techniques that measure the time-of-arrival (TOA) of sound signals have been reported to provide high accuracy ranging [8, 9, 10, 11, 12, 13]. Generally, for broadband systems, TOA is estimated by identifying the first peak of the matched filter implemented by correlating the band-limited filtered version of the ranging signal with its own reference copy, and counting the elapsed time samples. Depending on the propagation channel conditions, this mechanism introduces two uncertainties that can contribute to ranging inaccuracy due to error in estimating the correct correlation peak; first, it is normally surrounded by numerous sidelobes (adjacent peaks) that may attain approximately equivalent heights, and second, the envelope of the correlated signal is oscillating.

In this paper, we address many of these problems and demonstrate that ultrasound is also a good candidate for long distance ranging for both indoor as well as outdoor environments. Following are the main contributions:

- We use broadband ultrasonic chirps as a ranging signal, and study the impact of signal length and bandwidth on range and resolution, and related trade-offs.

- We propose a high accuracy ranging mechanism using a signal detection mechanism using the simple idea of estimating the envelope of the correlated (compressed) pulse that makes the role of sidelobes irrelevant, and counters the effect of noise through the least-square curve fitting approach.

- We present the design and implement two broadband ultrasonic ranging systems based on linear chirps. First, a PC-based system consisting of various COTS devices and custom designed units. Second, a Mote-based system using the CSIRO Audio nodes, which comprises of a Fleck-3z mote along with audio codecs and a Blackfin DSP. They, respectively, attain an operational range of 45m and 20m, and an average accuracy of approximately 2cm, with a maximum detection range of 57m and 30m.

We also illustrate practical challenges in the design and execution of our system, the lessons and experiences of which will be helpful to other engineers working on similar projects.

The rest of the paper is organized as follows: A review of related work is discussed in Section 2. Section 3 presents a general broadband signal analysis followed by a comparative study between linear/nonlinear chirps and PN signal. Section 4 discuses the system model of the proposed ranging system, and verifies the efficacy of the detection algorithm in simulation. Section 5 and Section 6 describes the design and implementation of the two proposed systems followed by their evaluation results. A comparison among existing systems is outlined in Section 8, and finally, a discussion of future work and conclusion is provided in Section 9.

2 Related Work

TOA-based acoustic systems fall into two categories depending on the available system bandwidth: *narrowband* and *broadband*. Broadband systems utilize a signal with relative bandwidth B_r ($= \frac{bandwidth}{center frequency}$) in excess of 20%. We refer our readers to our previous work in [17] where we have provided a detailed comparison of existing narrowband systems. The system proposed by Kushwaha et al. in [8], Hazas et al. in [18], AENSBox [9] and BeepBeep [10] are existing broadband systems. They share a common cross-correlation based signal detection technique, however, they differ in their signal design, synchronization schemes and methods to improve the received signal-to-noise ratio (SNR).

Kushwaha's system was based on the Mica2 platform with an attached custom 50 MHz DSP processor and an external speaker. The ranging signal was a Gaussian windowed linear chirp from 50 Hz-5 kHz. It employs a message timestamping technique. The SNR of the received signal is enhanced by adding a series of consecutive position-modulated chirps at the same phase and averaging these measurements.

The AENSBox system comprised of a custom designed acoustic sensor array that utilized beamforming to improve the received SNR, and time synchronization services to prevent clock skew and drifting. The ranging signal was a 2048-chip code modulated using binary phase shift keying (BPSK) on a 12 kHz carrier spread over 6-18 kHz. It differed from most of its predecessors in the use of separate synchronization service that maintained metrics to convert from one system clock to another on demand, rather than a synchronous radio and audio pulse. This approach is beneficial in scenarios where the audio range is greater than the radio range.

The BeepBeep system used a 50 ms linear chirp from [2-6] kHz. It used a two-way sensing scheme (different from the round-trip time measurements) to avoid clock synchronization, and was implemented on COTS mobile devices.

As these system operated in the audible range, they were not suitable for a general ranging strategy. Therefore, Hazas et al. proposed a broadband ultrasonic localization system that was implemented on custom designed Dolphin devices. The 25 ms ranging signal was generated using a 50 kHz carrier wave modulated by Gold codes (of length 511 bits) using BPSK. The sensitivity of the receiver was improved by using a transducer with a greater surface area (10 mm radius) rather than the general 5 mm transducer applied on the transmitter. The reported ranging results showed millimeter level accuracy that is comparable to the uncertainty in hand-measured distances, but it was only targeted for very short range (< 3 m) indoor applications. We compare the results of our system testing and related characteristics to some of the related work in Section 8.

3 Choice of Signal Waveform

Based on prior work in the field of acoustical localization in air, three classes of signal waveforms were identified: single tone sinusoidal, linear chirp, pseudo-noise (PN). Chirps are frequency modulated signals, where a sinusoidal wave of constant amplitude sweeps the desired bandwidth (B) within a certain time-period (T) in a linear or non-linear (for example following quadratic or logarithmic laws [19]) manner. PN signals are (phase) modulated sinusoidal waveforms mixed with pseudo-random sequences.

The time-period (T) and bandwidth (B) of the signal has a key role in delivering the desired coverage range and resolution. For observations and reasons reported in our previous work [17], we do not consider single tone sinusoidal signals. Broadband signals (chirps/PN), which utilize correlation based processing share a common theory on the BT relationship. In the following, we explain it for the linear chirp signal and then present our comparison studies for the remaining waveforms.

3.1 Linear Chirp Analysis

A linear chirp is represented by the bandpass signal:

$$s(t) = \begin{cases} cos(2\pi(f_0 t \pm \mu\frac{t^2}{2})) & \frac{-T}{2} < t < \frac{T}{2} \\ 0 & \text{elsewhere} \end{cases} \tag{3.1}$$

where, f_0 is the center frequency in Hz, and μ =B(Hz)/T(s) is the chirp rate that sweeps linearly from (f_0−B/2) to (f_0+B/2). The ± term defines its sweep direction. When the signal in (3.1) is passed through its matched filter, the following output is generated [20]:

$$g(t) \quad = \quad \frac{T}{2}\cos(2\pi f_0 t)\left[\frac{\sin(\pi\mu t(T-|t|))}{\pi\mu T t}\right] \quad \frac{-T}{2} < t < \frac{T}{2} \tag{3.2}$$

(3.2) is the approximate autocorrelation of the linear chirp $s(t)$ and it provides two important results:

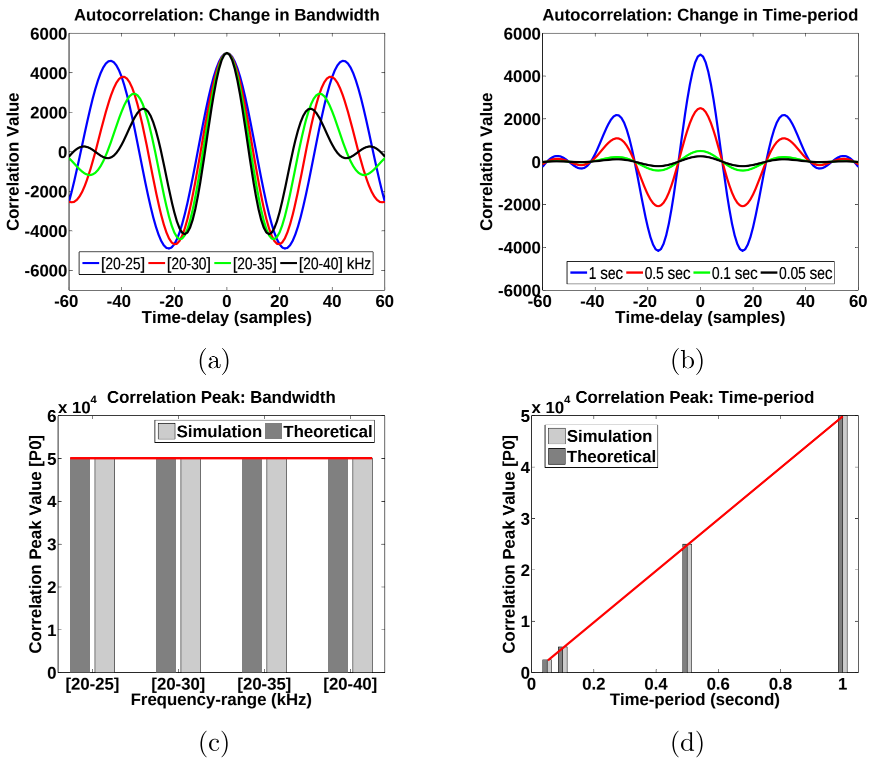

Figure 3.1: Theoretical Prediction vs. Simulation Measurements (*linear chirp*) on the effect of change in (a)-(c): Bandwidth (B) & (b)-(d): Time-period (T) on the Height and Width of the Correlation Peak.

- The *correlation envelope*, given by the term $\left[\frac{\sin(\pi\mu t(T-|t|))}{\pi\mu T t}\right]$ is approximately $\left[\frac{\sin(\pi\mu t T)}{\pi\mu T t}\right]$ for t <<T, with its first zeros at $t = \pm 1/(\mu \mathrm{T}) = \pm(1/\mathrm{B})$; and is inversely proportional to the bandwidth B (Figure 3.1(a) and (c)).
- The *peak value* (which signifies the energy of the signal) occurs at $t = 0$, and is proportional to the chirp length T (Figure 3.1(b) and (d)).

This gives the important relationship that *an increase in T increases the size of the post-correlation signal, and an increase in B gives better resolution by narrowing the envelope of the correlation peak.*

3.2 Chirp Waveform Comparison

In this section, we compare the various types of broadband chirps, and explain their features based on B and T.

For studying the change on bandwidth, four types of chirp (each of category: linear, quadratic and logarithmic) with constant time-period of 1 second and varying frequency range (and thus bandwidth) were designed: Chirp-1 [20-25kHz], Chirp-2 [20-30kHz], Chirp-3 [20-35kHz] and Chirp-4 [20-40kHz]. Figure

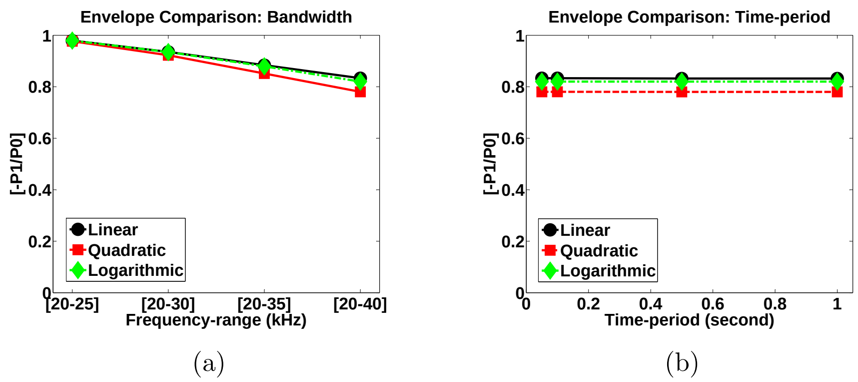

Figure 3.2: Linear vs. Quadratic vs. Logarithmic (Chirps). Effect of change in (a): Bandwidth (B) & (b): Time-period (T) on the characteristic of the Correlation Envelope.

3.1(a) and (c) compares the theoretical prediction with the simulation measurements (for linear chirps) with respect to B and the height of the correlation peak [P0]. It shows a perfect match for all the different chirps-[1/2/3/4], and hence, establishes the correctness of the generated signal. We observe that [P0], which signifies the energy of the signal, is the same for all the chirps. Figure 3.2(a) shows the ratio between the height of the first negative peak [-P1] to the correlation peak [P0] denoted as [-P1/P0] for linear, quadratic and logarithmic chirps for the different types (chirp-[1/2/3/4]). These peaks are related to the envelope of the correlation output, which is an important factor. A lower ratio of [-P1/P0] signifies a narrower correlation envelope, and is best supported by the highest bandwidth signal (i.e. Chirp-4). The linear and logarithmic chirps have similar correlation envelopes; however, the envelope cover of the quadratic chirp is even narrower. This suggests that although B does not define the acoustic pressure level of the chirp, yet a higher bandwidth signal is preferable due to its narrower correlation envelope that can improve the resolution of the range measurement.

Similarly, for the studying the change in time-period, four types of chirp were designed with constant bandwidth of 20kHz and varying time-periods: Chirp-1 [1s], Chirp-2 [0.5s], Chirp-3 [0.1s] and Chirp-4 [0.05s]. Figure 3.1(b) compares the theoretical prediction with the simulation measurements (for linear chirps) with respect to the T and the height of the correlation peak [P0]. We observe that [P0] increases proportionally with the increase in T, where it is maximum for Chirp-1 and minimum for Chirp-4. This difference in peak values suggests that signal duration should be chosen to match the ranging requirements, although at the cost of extra computation for processing a longer signal length. Figure 3.2(b) shows that [-P1/P0] is constant for all the different chirps, which suggests that the correlation envelope remains constant with the change in T, and hence is independent of the time-period, irrespective of the chirp type (linear, quadratic, logarithmic).

3.3 Discussion

The compression aspect of the chirp pulse comes from the fact that while the transmitted pulse is rectangular with unity voltage and duration $\frac{-T}{2} < t < \frac{T}{2}$, the output of the matched filter has most of the energy from $\frac{-1}{B} < t < \frac{1}{B}$ and a peak voltage of $T/2$. As T controls the peak value of the correlated signal, one may consider choosing a longer signal duration that has higher energy to travel longer distances. However, a longer ranging signal increase the system reaction time, wherein the pulse repetition frequency has to be kept low; which means that the entire system is required to wait for one signal and all its echoes to decay before transmitting the next pulse. Second, it increases the overall system cost, in terms of processing time, energy consumption and storage, thereby making its implementation difficult on resource-deficient sensor motes. B determines the width of the correlation envelope, and therefore, determines the range resolution. Although, working in the ultrasonic domain provides the flexibility to use band of signal frequencies above 20kHz, higher frequencies components are more vulnerable to atmospheric absorption. This limits the use of an ultra-wide bandwidth ultrasonic signal. The appropriate choice of B and T depends on the application requirements, but from the study presented in the previous subsection, it appears reasonable to choose a broadband signal of the *highest bandwidth* (for best detection accuracy), and *shortest time-period* (for long-range incurring the least cost).

With regards to the choice between linear/non-linear chirps and PN signal, we generated a 20-40 kHz/1 s pulse for each category, and compared them on the basis of their individual envelope cover (height of the first negative peak [-P1] and first positive peak [+P1] to the correlation peak [P0]) and spectral complexity. For a PN signal of certain B and T, we observed that the correlation (peak and sidelobes) properties vary across different pseudo-random numbers, and therefore, we calculated the running average across 1000 randomly chosen PN codes.

Table 3.1 summarizes the overall statistics. A lower value of [-P1/P0] and [+P1/P0] signifies a narrower signal envelope, and is best supported by chirp waveforms than PN signals. With regards to the spectral complexity (observed by a spectrogram), the linear chirp is the simplest of all. In this work, we do not make use of the spectral characteristic of this waveform; however, we intend to take advantage of this feature to improve detection accuracy in our further work. Hence, based on these requirements, we decide to use a *linear chirp* as our ranging signal.

In the following section, we discuss the system model, and present a simulation study of the ranging performance of linear chirps with our proposed detection algorithm.

Table 3.1: Chirps vs. PN Signal Characteristics

Signal Type	**[-P1/P0]**	**[+P1/P0]**	**Complexity**
Chirp (Linear)	0.8332	0.4358	Low
Chirp (Logarithmic)	0.8201	0.3961	High
Chirp (Quadratic)	0.7802	0.3030	High
Pseudo-noise	0.8106	0.6211	High

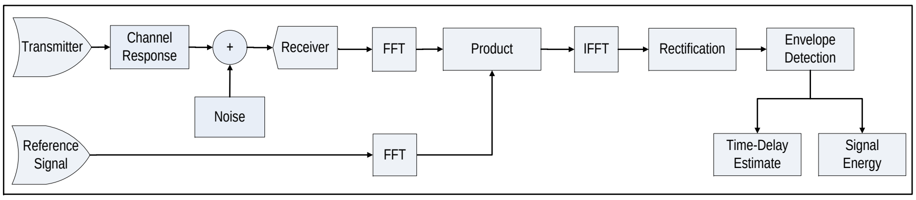

Figure 3.3: Block Diagram: Acoustic Channel Model & Signal Detection Algorithm.

4 System Model

We represent an indoor environment using a reverberation geometrical acoustic model [19](Figure 3.3). For the mathematical formulation, we adopt the following notation: $s(t)$ and $d(t)$ represent the signal emitted by the transmitter(Tx) and received at the receiver(Rx) respectively; the respective impulse responses of the transmitter, environment (channel) and receiver are represented by $h_{tx}(t)$, $h(t)$ and $h_{rx}(t)$; and the white Gaussian noise in the channel is denoted by $v(t)$.

$s(t)$ is a broadband signal in the form of a linear chirp, and is transmitted at $t = 0$ by Tx. The signal $d(t)$ received at Rx is the convolution:

$$d(t) = s(t) * h_{tx}(t) * h(t) * h_{rx}(t) + v(t) * h_{rx}(t)$$

Assuming $h_{tx}(t)$ and $h_{rx}(t)$ are of unit magnitude (i.e. neither the transmitter nor the receiver change the signal characteristics):

$$d(t) = s(t) * h(t) + v(t) \tag{4.1}$$

$h(t)$ is modeled as the sum of $M + 1$ impulses corresponding to the direct path with propagation delay τ_0, and M other possible paths between Tx and Rx as:

$$h(t) = \sum_{i=0}^{M} A_i \delta(t - \tau_i)$$

where A_i is the amplitude of the i-th ray, and $\delta(t - \tau_i)$ represents the delay in propagation from Tx to Rx. Ray $i = 0$ is defined here as the direct sound ray from the source to the receiver, and rays $i > 0$ are defined as reflected rays. $\tau_i = d_i/c$, where d_i is the distance traveled by ray i, and c is the speed of sound under room conditions.

4.1 Signal Detection and Post-processing

The received signal $d(t)$ is processed using a matched filter implemented by correlating it with a reference signal $s(t)$ (i.e. a locally stored copy of the originally emitted signal), and result in:

$$\begin{aligned} y(t) &= [d(t) \star s(t)] \\ y(t) &= [s(t) * s(-t)] * h(t) + v(t) * s(-t) \end{aligned} \tag{4.2}$$

$y(t)$ has its earliest component $[s \star s](t - \tau_0)$ (where: $\star$ implies correlation), whose peak can be used to determine τ_0 (direct path signal) with considerable precision, provided the other multipath components of $d(t)$ are sufficiently weak, and/or separated in time from $t = \tau_0$. The noise term $v(t) * s(-t)$ may result in the shifting of the peak at τ_0 from its actual time-line. This may result in deviation of the distance estimation results.

The signal detection scheme discussed in existing work provide resistance to multipath and low-noise signals [8, 18, 9, 10] by using a peak detection approach, which under the condition of a direct line-of-sight (DLOS) between the transmitter and receiver, identifies the first tallest correlation peak that exceeds a preset threshold. However, from our study and observations, we noticed two potential problems. First, the correlation peak is surrounded by numerous sidelobes (i.e. adjoining peaks). Second, the correlation plot obtained from processing the band-limited signal is highly oscillating in envelope cover. Both these conditions provide an inaccurate estimate of the correct detection peak in the vicinity of similar peaks of approximately equivalent heights under noisy conditions. Therefore, we propose a simple envelope detection mechanism that makes the role of sidelobes irrelevant, and counters the effect of noise and envelope oscillations through the least-square curve fitting approach. In addition, it also provides the benefit of finer resolution that can be fractions of a sampling period.

The envelope detection approach estimates the maximum value of the envelope of the compressed (correlated) pulse that should give the best estimate of its position. A simple least-squares approximation technique has been used to find the envelope of the rectified signal, rather than the standard approach of calculating the magnitude of the analytical signal. The algorithm identifies the position of the local peak (t_2, y_2) that is greater than its left and right neighbor peaks at (t_1, y_1) and (t_3, y_3), finds the parabola that passes through these points exactly, and finally, calculates the time coordinate of the maximum of this parabola ($t = t_{peak}$). Therefore, fitting a parabola to these three points requires solving the following system of three linear equations for the three unknown $[a, b, c]$:

$$\begin{aligned} y_1 &= at_1^2 + bt_1 + c \\ y_2 &= at_2^2 + bt_2 + c \\ y_3 &= at_3^2 + bt_3 + c \end{aligned}$$

The corresponding representation in matrix form is:

$$\mathbf{A}\hat{\mathbf{x}} = \mathbf{B}$$

where $\hat{\mathbf{x}} = [a\ b\ c]^T$ is the matrix of unknown parameters, and:

$$\mathbf{A} = \begin{bmatrix} t_1^2 & t_1 & 1 \\ t_2^2 & t_1 & 1 \\ t_3^2 & t_1 & 1 \end{bmatrix}$$

$$\mathbf{B} = [y_1\ y_2\ y_3]^T$$

Thus, $\hat{\mathbf{x}} = \mathbf{A}^+\mathbf{B}$, where $\mathbf{A}^+$ is the inverse matrix of $\mathbf{A}$. The maximum of the envelope occurs at $t_{peak} = -b/(2a)$.

In case of low-noise signals, there are more peaks surrounding the highest peak as shown in Figure 4.1-(a). The parabolic curve fitting using least-square approximation technique does the best to pass as near as possible to all the adjacent peaks, and thus, provides resistance to noise on the data points. To illustrate the least-square approximation process, suppose there are n data points that can be modeled by a system of n quadratic equations for the three unknown coefficients $[a, b, c]$. If n is greater than the number of unknowns (i.e. 3), then it is an overdetermined system, and is solved by the least-square parabolic fitting process that minimizes the summed square of the residuals. Let the difference e_i between the i^{th} data point (t_i, y_i) and the fitted parabola be:

$$e_i = y_i - (at_i^2 + bt_i + c) \tag{4.3}$$

Then, the sum of squared errors is given by:

$$E = \sum_{i=1}^{n} e_i^2 \tag{4.4}$$

The goal is to minimize E, and is determined by differentiating E with respect to each parameter (or unknown), and setting the result to zero (i.e. $\partial E/\partial a = \partial E/\partial b = \partial E/\partial c = 0$) Thus, we obtain the following three equations for the three unknowns $[a, b, c]$:

$$\sum_{i=1}^{n} y_i t_i^2 = a \sum_{i=1}^{n} t_i^4 + b \sum_{i=1}^{n} t_i^3 + c \sum_{i=1}^{n} t_i^2 \tag{4.5}$$

$$\sum_{i=1}^{n} y_i t_i = a \sum_{i=1}^{n} t_i^3 + b \sum_{i=1}^{n} t_i^2 + c \sum_{i=1}^{n} t_i \tag{4.6}$$

$$\sum_{i=1}^{n} y_i = a \sum_{i=1}^{n} t_i^2 + b \sum_{i=1}^{n} t_i + cn \tag{4.7}$$

This linear system can be solved (as explained before) for $[a, b, c]$ to provide an estimate for the position of the peak: $t_{peak} = -b/(2a)$. t_{peak} is the estimate of the pulse position, and thus, provides a range estimate.

4.2 Simulation Results

We simulated a custom environment in MATLAB, and evaluated the performance of the proposed ranging algorithm. The simulator was designed to construct a virtual 2D rectangular room with (top,left) and (bottom,right) coordinates as: $(-5, \zeta/2)$ and $(\zeta + 5, -\zeta/2)$ respectively, where ζ is the distance between Tx and Rx, and is varied from 1-20 m for every set of measurements. Tx and Rx were placed at positions $(0, 0)$ and $(\zeta, 0)$. It was configured to generate fixed number of reflection points at random positions in the enclosed geometry, and was programmed as per the described system model.

Measurements were taken at different positions inside the room for distances between 1-20 m. Every simulation was run for a length of 1000 iterations. The simulator was configured for 5 reflection points with attenuation factor of 0.9, and the transmitted signal of [20-40] kHz/50 msec (sampled at 96 kHz) was added with white Gaussian noise (SNR=10).

Figure 4.1-(a) shows the output from the correlation function, the result of rectification and envelope detection of the correlated pulse. Figure 4.1-(b)

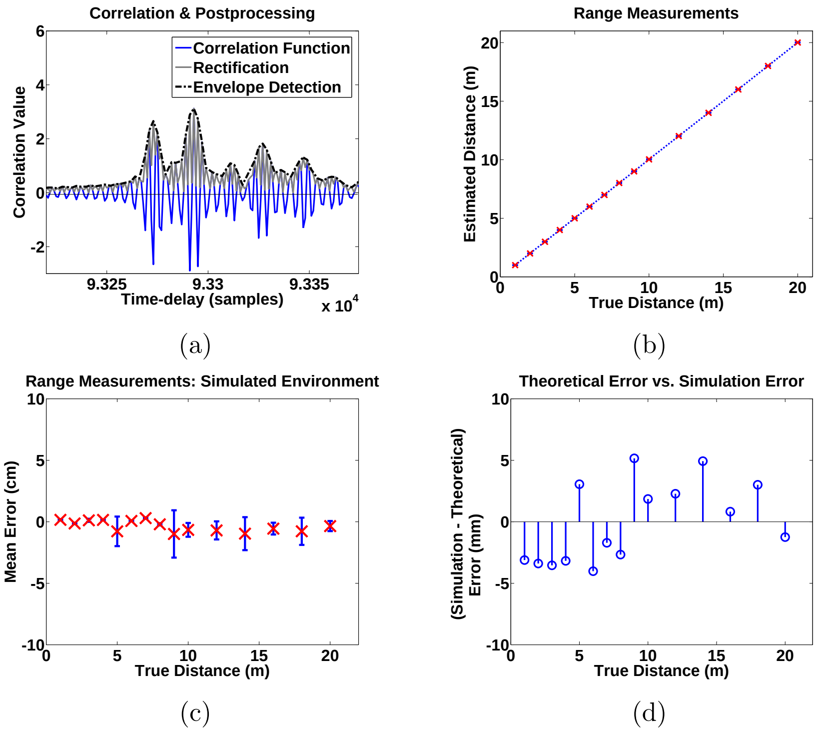

Figure 4.1: (a): Signal Detection and Post-processing. Simulation Results for Range Estimation. (b): True Distance vs. Estimated Distance. (c): Mean error with vertical bars representing 95% confidence intervals. (d): Theoretical error vs. Simulation error.

and (c) shows the distance estimation accuracy obtained from the simulation measurements. We observe that the magnitude of the mean errors is consistently less than 1cm for distances upto 20 m. Figure 4.1-(d) plots the difference between errors derived from simulation and their respective theoretical prediction [20] for distance measurements of Figure 4.1-(c). A positive error denotes that the error incurred from simulated measurements are more than their predicted theoretical value, and vice-versa for negative errors. It shows that there is an average difference of 3mm between the simulated and predicted errors for all the measurement points, with a maximum deviation of 5 mm. Therefore, we conclude that our detection methodology is precise enough for fine-grained ranging.

5 PC-based System Implementation

The acoustic ranging system consists of four separate units: processing, data acquisition, sensor and actuator. All these units have been used separately without assembling them onto a single device. The idea is to experimentally verify the feasibility of the proposed scheme using separate entities, before incorporating them into an embedded system. In this manner, we hope to derive the

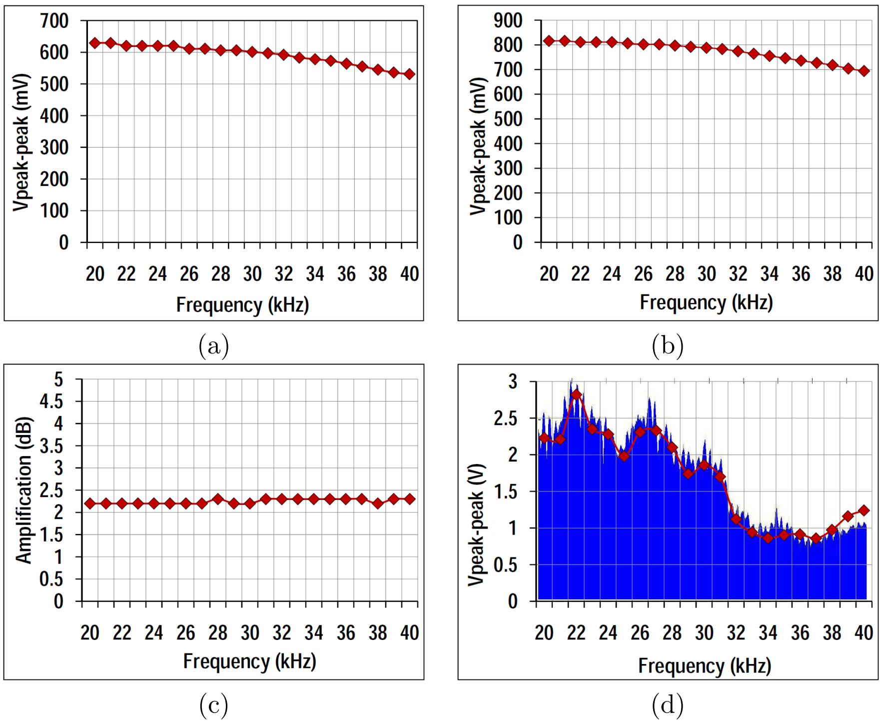

Figure 5.1: Device Characterization. (a):Frequency response of the audio-card. (b):Amplification level of the amplifier. (c):Frequency response of the amplifier. (d): Frequency response of the receiver.

best performance of our ranging system, by having control over every system component. These devices have not been fully optimized for size and power.

5.1 Hardware Components

Provisioning a system in the ultrasound space requires a data acquisition (DAQ) board capable of sampling at a minimum rate of twice the highest operational frequency of 40kHz, and high resolution for faster signal processing. Our DAQ unit, therefore, consists of the XONAR D2X audio card [21] that has a wide frequency span from $<$ 10Hz to 46kHz, and supports a sampling frequency/resolution of 96kHz/16 bit. Figure 5.1-(a) shows its frequency response in the range from [20-40]kHz. It is approximately flat with a minor drop of $\approx$ 1.5dB.

Piezoelectric ceramic transducers have been widely used as a sensing element in existing narrowband ultrasonic location systems [15, 16], primarily due to their high sensitivity within the realm of small form-factor and low-cost; however, they have a usable bandwidth of $\approx$ 2-5kHz. Hence, [18] used piezo film transducers, but has reported them to be less efficient in maintaining a constant peak-to-peak voltage across the entire frequency range, and therefore, used an additional step-up transformer unit to match the drive signal levels.

Leveraging on these lessons, we used an off-the-shelf ribbon (speaker) trans-

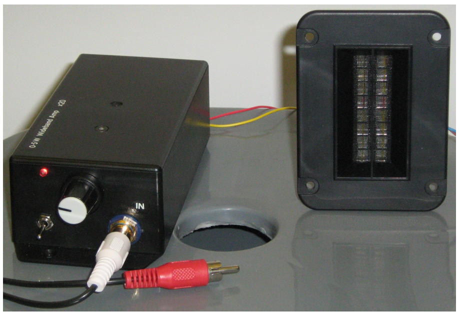

(a): Speaker and Amplifier.

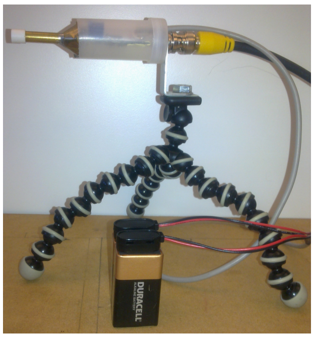

(b): Microphone.

Figure 5.2: Ranging Components of the PC-based System.

ducer (wherein the quick acceleration of the light-weight ribbon driver provides good high-frequency response) driven by an external wideband (power) amplifier (Figure 5.2-(a)) to provide flexibility during experiments. The amplifier is a light-weight portable unit that is powered by batteries, and has a tunable gain controller [5x-20x]. It records a consistent amplification level of 2.2/2.3dB over the entire frequency span (Figure 5.1-(b)), and shows a fairly flat frequency response (Figure 5.1-(c)).

Compared to the less efficient but commonly used piezoelectric ceramic/film transducers, we choose a MEMS surface mount wideband ultrasonic sensor from Knowles Electronics (part number SPM0204UD5 [22]), primarily due to its omni-directionality, high sensitivity and SNR within an extremely small form factor of 4.72mm $\times$ 3.76mm $\times$ 1.40mm. The implemented receiver is shown in Figure 5.2-(b). The frequency response of the receiver (Figure 5.1-(d)) was characterized by placing it in close proximity (i.e. 10cm) to the speaker, and measuring its response at different frequency levels. Therefore, the total signal measured at the output of the microphone includes all the effects of the audio-card, wideband amplifier, (short) propagation channel, receiver microphone and receiver amplifier. In the related figure, the blue part shows a horizontal cross-section of the received chirp signal, while the red (envelope) line is the frequency response. We observe that there is a close similarity between the two traces, which establishes the correctness of our result. It depicts a non-flat envelope with frequencies from 32-40kHz getting more attenuated than 20-31kHz.

5.2 Experimental Signal Analysis

The same four types of linear chirp were generated as mentioned in the previous sections. Figure 5.3-(a) compares the experimental measurement with the simulation result and the theoretical prediction for the height of the correlation peak [P0] with respect to B. As the experimental chirp is an amplified version of the regular simulated chirp, the curve is expected to be approximately straight with a greater magnitude; however, it has a linearly decreasing trend with increasing B with the maximum and minimum [P0] occurring for Chirp-1 and Chirp-4 respectively. As these measurements were taken at the receiver that attenuates higher frequency components [32-40kHz] more than lower frequency

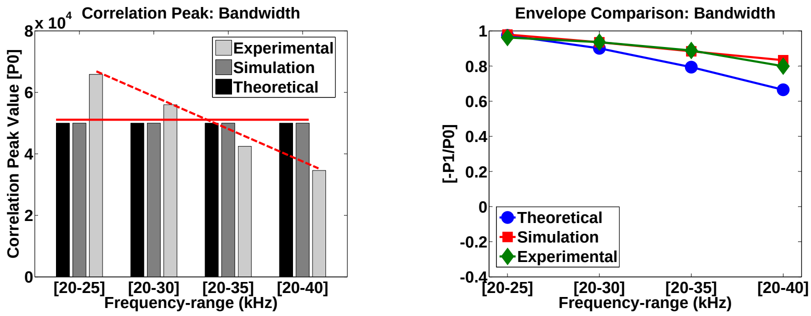

(a) (b)

Figure 5.3: Theoretical vs. Simulation vs. Experimental Measurements on the effect of change in Bandwidth on the (a): Height of the Correlation Peak. (b): Correlation Envelope.

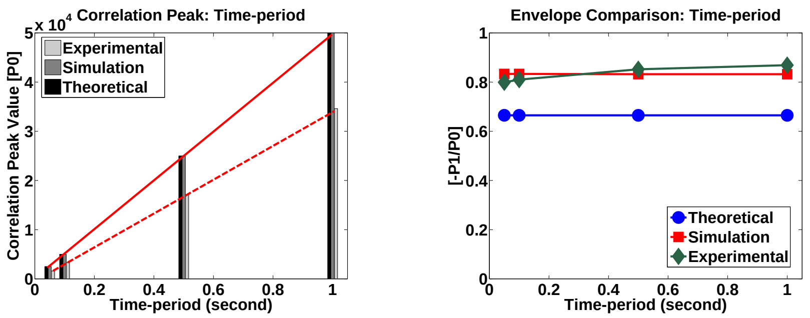

(a) (b)

Figure 5.4: Theoretical vs. Simulation vs. Experimental Measurements on the effect of change in Time-period on the (a): Height of the Correlation Peak. (b): Correlation Envelope.

components [20-31kHz](Figure 5.1-(d)), therefore, [P0] drops for Chirp-3 & 4. From Figure 5.3-(b) we observe that the width of the correlation envelope (indicated by [-P1/P0]) of the experimental chirps is approximately the same as the simulation result, but is not as good as the theoretical prediction. However, experimental [-P1/P0] is approximately close to 80%, and therefore, provides a satisfactory scope for good detection.

The same four types of linear chirp were generated as mentioned in the previous sections. Figure 5.4-(a) shows that the peak correlation [P0] of the experimental chirps are still proportional to their time-periods; however, the increase in the peak heights are below the expected values as predicted from the theoretical and simulation results. Figure 5.4-(b) shows that the correlation envelope of the experimental chirp is approximately the same as their values expected from simulation. Again, as noticed before, the correlation envelope remains constant with the change in T, and hence is independent of the time-period.

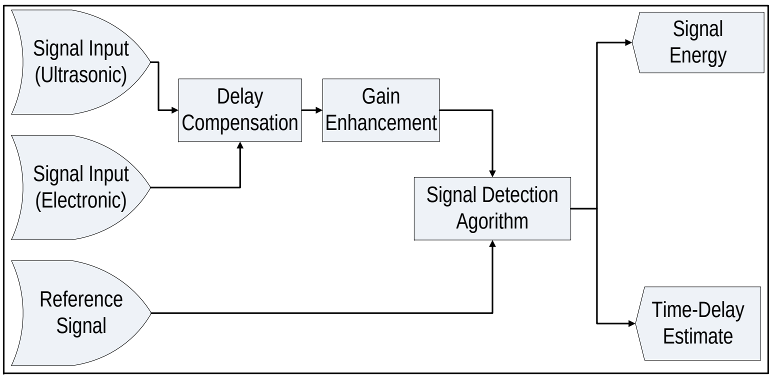

Figure 5.5: Block Diagram: Experimental Range Estimation.

From this study, we conclude that the characteristics of the experimental chirps are as expected from their theoretical prediction and simulation measurements, and do not deviate to the extent that they require calibration.

5.3 Range Estimation

The proposed broadband ultrasonic ranging system is an active, cooperative ranging system. A high-level description of the ranging methodology consists of measuring the time-difference-of-arrival (TDoA) between two synchronous RF and ultrasonic signal. Figure 5.5 shows the block digram of the experimental range estimation procedure.

In our implementation, signals are generated, captured and analyzed using a workstation PC. A digital linear chirp in the range [20-40]kHz and time-period 50msec is generated through the software (MATLAB). It is converted into its analog form by the DAC of the audio card, and then, directed into two separate streams: (a) I/P channel-1 of the ADC of the audio card, and (b) wideband amplifier. The electronic chirp (directed into the ADC) is equivalent to an RF pulse and marks the time of transmission of the chirp signal, while the amplified signal is emitted by the speaker. The ultrasonic chirp is detected by the receiver and directed into I/P channel-2 (Figure **??**) of the ADC in the audio card where it is digitized and queued for processing. The processing stage compensates for the transmission delay, enhances the signal through software gain control and performs the envelope detection to estimate the time-of-flight of the ultrasonic chirp.

Depending on the height of the received signal envelope, the software gain controller amplifies the received samples. The final acoustic signal is considered from the time-of-arrival (ToA) of the electronic chirp. It is detected using a matched filter implemented by correlating it with a reference signal, followed by rectification and envelope detection as explained in Section 4.1.

Autocorrelation Noise and System Calibration

We examine the distribution of autocorrelation noise for our linear chirps by placing the transmitter in very close proximity with the receiver (no physical gap), and performing a series of ranging experiments. The reference signal was correlated with a copy of the reference after passing through the system that included distortion induced by the audio-card, transmitter, amplifier, speaker and the connecting cables. Therefore, the characterization of the system noise is a combination of the system and autocorrelation noise.

Figure 5.6-(a) shows the distribution of correlation values that fits a normal distribution with a perfect mean of 0 and variance of 0.47. There are no trailing data points in this distribution, which suggest that there are no major errors induced by the hardware platform, but there is a certain system delay due to the signal propagation through the long connecting cables. Interestingly, there is an small intervening channel between the transmitter and the receiver, as their acoustic sensitivity regions do not appear near the physical outer limits, but are situated at some distance inside the devices.

Next, we calibrate our system to account for this time-delay. A series of ranging experiments are conducted for distances from 5cm to 100cm. Figure 5.6-(b) shows the distribution of corresponding range estimation errors with a mean error of 12.51mm. This constant bias was negated from range measurements to remove the system induced error. As the speaker body is 12mm thick and the ultrasonic transducer element on the receiver is 1.4mm deep, it suggests that this lag was primarily due to the acoustic sensitivity points being situated at the end of the respective transducer elements.

5.4 Experiments and Results

To evaluate the performance of our system, we conducted a range of indoor and outdoor experiments. Indoor environments are reverberant and cause multiple reflections. Outdoor environments are affected by weather conditions, where wind, temperature and relative humidity affect the measurement accuracy. Variations in the temperature are difficult to measure with accuracy required to achieve millimeter precision. In addition, its correction is dependent on the average temperature along the path between the transmitter and the receiver, and not at any single point.

Based on these facts, we choose experimentation regions where the environmental factors were relatively uniform. We choose a bright sunny day with less

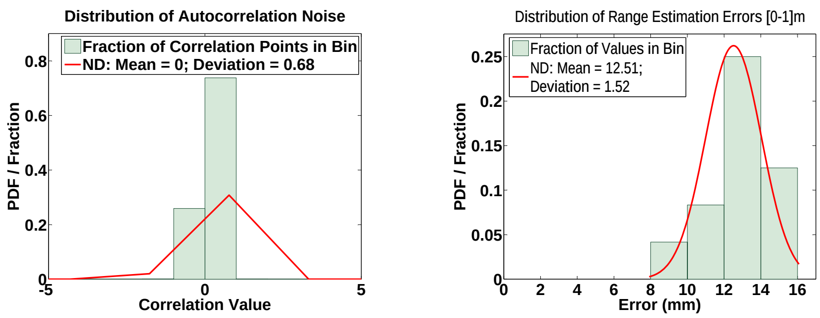

(a) (b)

Figure 5.6: (a): Autocorrelation noise. (b): System calibration.

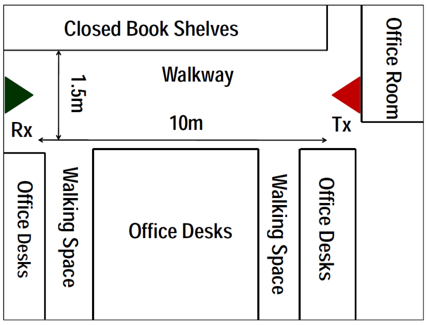

(a): Case-A

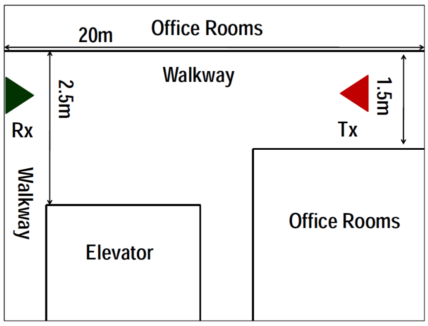

(b): Case-B

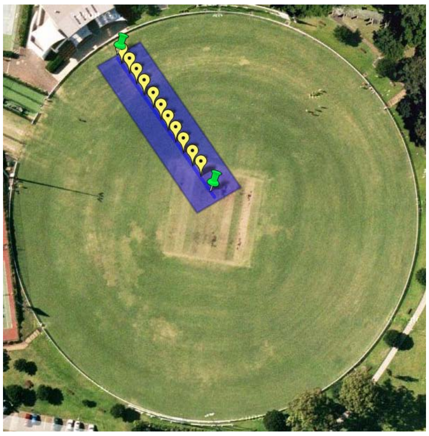

(a): Case-C

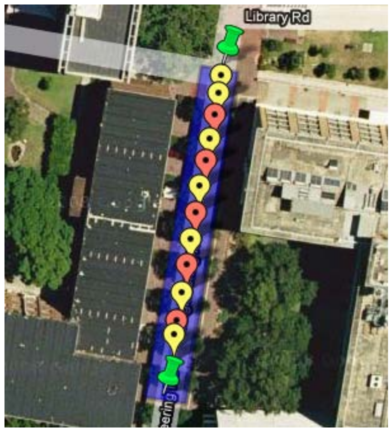

(b): Case-D

Figure 5.7: Testbeds for the ranging experiment.

wind movement, and performed each set of experiments in a short time span during which it is assumed that the changes in the environmental factors are minimal. The temperature readings were taken at both the transmitter and the receiver, and then averaged to obtain the final temperature for each experiment. In all our experiments, the receiver was fixed while we performed a controlled and careful movement of the transmitter using a measuring tape, markers and a pair of Cricket motes (for measuring every successive meter) for establishing the correct ground distance. The microphone receiver was shielded with a windscreen to reduce the effect of wind movement on the measurements.

The system is evaluated under four environments:

Case-A - Indoor, Noisy: Research Lab ($10m \times 1.5m \times 5m$) (Figure 5.7-(a)).

Case-B - Indoor, Quiet: Corridor ($20m \times 2.5m \times 5m$)(Figure 5.7-(b)).

Case-C - Outdoor, Open-ground: Oval (Figure 5.7-(c)).

Case-D - Outdoor, Urban: University Walkway (Figure 5.7-(d)).

In our experiments, the speed of sound used in distance calculation is according to the model: $c_{air} = 331.3 + 0.6\theta$, where 331.3 is the speed of sound at 0^oC and θ is the air temperature in Celsius (^oC). We also plot the probability den-

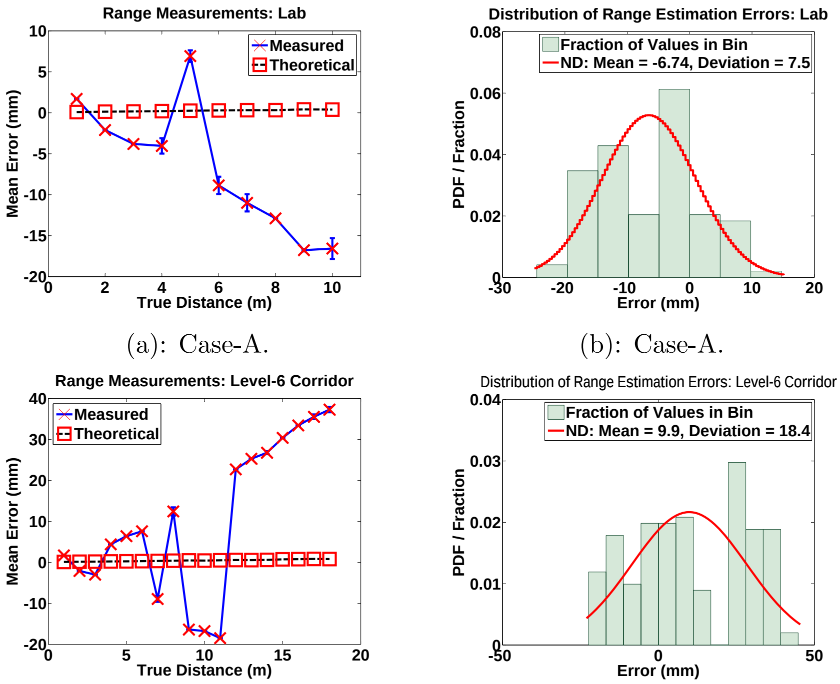

(a): Case-A. (b): Case-A.

(c): Case-B. (d): Case-B.

Figure 5.8: Indoor experiments.(a)&(c): Range estimation error relative to ground truth. The vertical bars represent 95% confidence intervals.(b)&(d): Distribution of errors.

sity function of the ranging errors as a histogram for all the experiments to get a aggregate view of the performance of our system under different conditions. In practice, prior distance information would not be available, hence the error distribution shows the accuracy that can be achieved with multiple experiments.

Indoor

Figure 5.8-(a) shows the accuracy measurements for different distances for Case-A settings. The mean ranging error shows millimeter accuracy < 10mm for distances upto 6m, with a maximum mean error < 17mm at a distance of 10m. The ranging results are highly stable with a standard deviation of ≈ 0 for most of the measurements, with a maximum value below 2mm. The distribution of the range estimation error is shown in Figure 5.8-(b), and it fits a normal distribution with a mean error of 6.74mm and standard deviation of 7.5mm.

Figure 5.8-(c) shows the accuracy measurements for different distances for Case-B settings. The ranging accuracy is comparable with Case-A for distances upto 10m, and then shows a moderate increase in mean error to 3.8cm at its maximum range of 18m. Again, these results show great stability with ≈ 0 standard deviation for a majority of the measurement points, and attains a maximum deviation of 3mm. These deviations occur more frequently after a distance of 10m, which is mostly accountable to the geometry of the room and

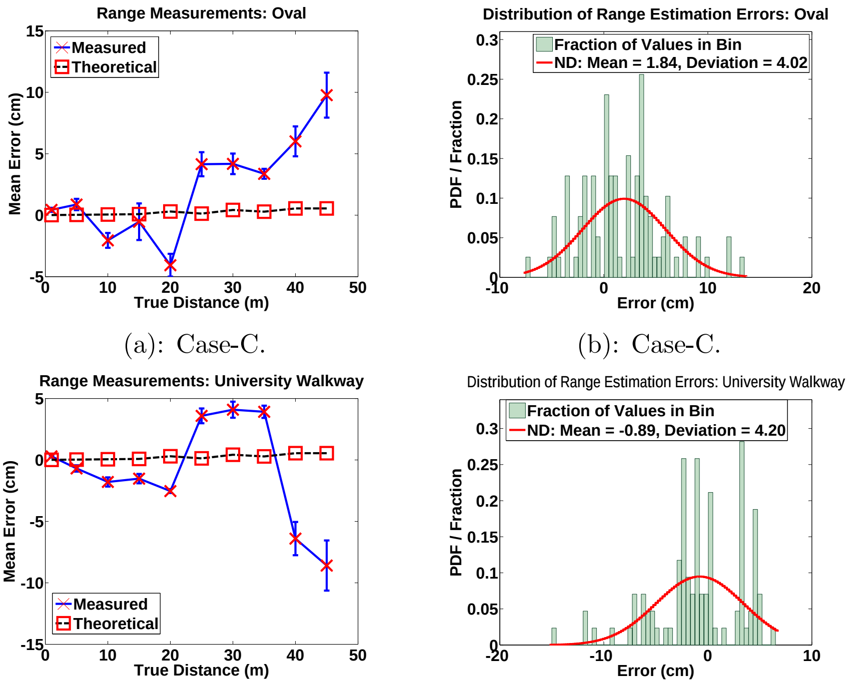

(a): Case-C. (b): Case-C.

(c): Case-D. (d): Case-D.

Figure 5.9: Outdoor experiments.(a)&(c): Range estimation error relative to ground truth. The vertical bars represent 95% confidence intervals.(b)&(d): Distribution of errors.

the channel length, more than the decrease in SNR. The distribution of the range estimation error is shown in Figure 5.8-(d), and has a normal distribution with a mean error of 9.9mm and standard deviation of 18.4mm. It has an excess of overestimates (range estimates longer than true distance) that may be due to the multipath effect where the microphone does not detect the signal until long after it actually arrives.

Outdoor

The accuracy measurements Case-C and Case-D are shown in Figure 5.9-(a) & (c) respectively. The error distributions for the respective settings are also shown in Figure 5.9-(b) & (d). We observe that with the exception of a few measurements, the magnitude of the error is consistently below 5cm. While on an individual measurement basis, the mean ranging errors for Case-C are between [-5cm, 10cm] and those for Case-D are within [6cm, -8cm], but their overall (system) mean error is respectively 1.84cm and -0.89cm. Also, their individual standard deviations vary between [0.03cm, 2cm] and [0.16cm, 3cm] for Case-C and Case-D respectively, but have a system level deviation of 4.02cm and 4.20cm. The error distribution shows greater data points in the region of underestimates (range estimates shorter than true distance) which is due to the microphone detecting the ultrasound pulse before it actually arrives, perhaps due to the outdoor environmental noise. The maximum reliable operational range recorded for both Case-C and Case-D is 45m. In fact, a significant number of distance estimates were recorded at distances as far as 57m, but they were highly erroneous with no significant correlation.

Evaluation Summary

Table 5.1 summarizes the statistics for all the experiments. The absolute value for mean and standard deviation has been used for calculation. The table shows that the proposed ranging system indeed leads to high accuracy (¡ 2cm) ranging results and works reliably in all the test cases. The maximum reliable operational range is 45m, and as long as the devices are within this scope, our system works reliably. Although the theoretical accuracy (Figures 5.8-(a)&(c) and Figures 5.9-(a)&(c)) for all the tests are of the order of sub-millimeter, the ranging accuracy obtained from measurement results are in the sub-centimeter scale. But, it is important to note that the mean of the distribution errors for the indoor experiments are indeed below 1cm, while those for the outdoor experiments are below 2cm. Figure 5.10 shows the cumulative distribution of the range estimation errors for all the four test cases. It shows that with the exception of a few cases, the majority of these measurement points (or errors) are always within 5cm with a probability of 80%.

Table 5.1: Summary

Environment	Operational Range (m)	Overall Mean Error (cm)	Overall Deviation (cm)
Case-A	10	0.67	0.76
Case-B	18	1.00	1.8
Case-C	45	1.84	4.02
Case-D	45	0.89	4.20

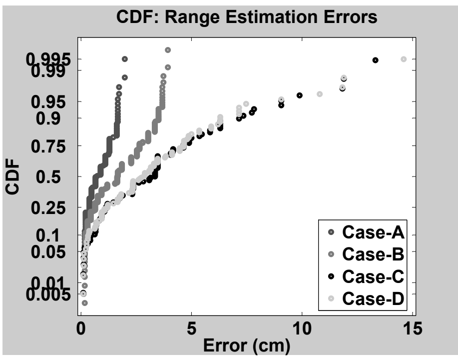

Figure 5.10: CDF of the Range Estimation Errors.

6 Mote-based System Implementation

6.1 System Design: Hardware & Software

This system has been implemented on CSIRO Audio nodes using its wireless sensor network platform: the Fleck-3z. Its main components include the Atmega1281 microcontroller, 1 MB external flash memory, and a low-bandwidth Atmel RF212 radio transceiver operating in the 900 MHz band (Figure 6.2). It supports a flexible range of digital I/Os and a daughter board interface, which allows the use of expansion boards to enhance its base functionality. The architecture relies heavily on the SPI bus, where the microcontroller acts as the SPI master and communicates with the remaining system components over the SPI interface.

(a)

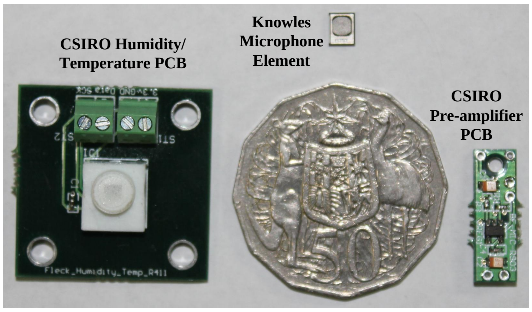

(b)

Figure 6.1: System Components

The audio signal processing daughter board (designed by CSIRO) was used for ultrasonic ranging (Figure 6.1(a)). It includes four TI TLV320- AIC3254 audio codecs, each providing two audio I/O channels along with internal functionalities such as programmable gain amplifiers and software configurable filtering; micro SD flash memory card slot, and a connector to hold the CM-BF537E digital signal processor module manufactured by Bluetechnix. The CM-BF537E module combines a (Analog Devices) Blackfin DSP running at up to 600 MHz, a 32 MB RAM and an Ethernet interface. The DSP communicates with the Fleck microcontroller through a serial interface. The current consumption of this daughter board is in excess of 200 mA in the active state, and so (in its current implementation) Fleck-3z mote controls power to this board ensuring that the relatively high power consumption is only incurred during audio transmission and acquisition. There are two simple daughter boards that provide connector access to the audio I/O ports and an Ethernet socket.

The transmitting front-end of the beacon mote consisted of a power amplifier driving a tweeter (speaker) transducer (VIFA 3/4" tweeter module MICRO). It was chosen due to its small size ([2×2×1] cm) and good high-frequency response, compared to existing broadband transducers or piezoelectric ceramic/piezo film transducers (reported in existing literature). The amplifier is a light-weight portable unit with a maximum output power of 0.5 W. It is powered by batteries and has a tunable gain controller.

The receiving front-end of the listener mote consisted of the Knowles micro-

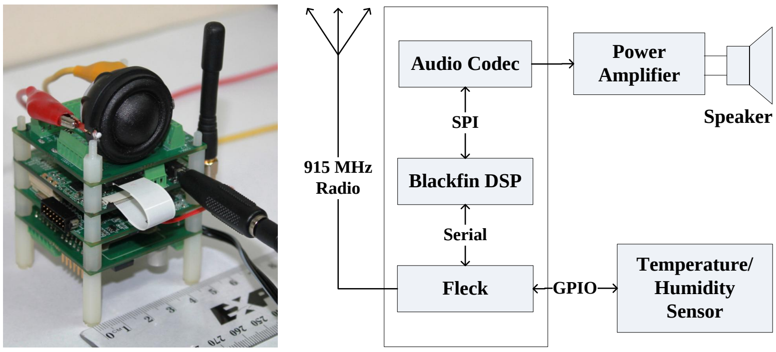

(a) (b)

Architecture of the Beacon.

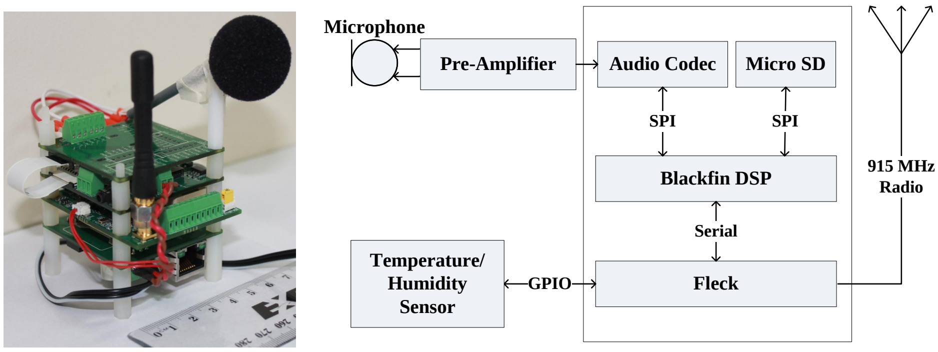

(a) (b)

Architecture of the Listener.

Figure 6.2: Mote-based Ranging System.

phone (SPM0404UD5 [19]) fixed to the pre-amplifier PCB designed by CSIRO (Figure 6.1(b)). The surface mount wideband ultrasonic sensor was chosen due to its omni-directionality, high sensitivity and SNR within an extremely small form factor of $[4.72 \times 3.76 \times 1.40]$ mm. The small PCB has been designed operate in close proximity with the microphone in order to minimize the susceptibility of the low amplitude microphone output signals to corruption by electrical noise. Figure 6.3 shows the frequency response characteristics for both the transmitting and receiving front-ends, which have an approximately 20 dB acoustic pressure level above the noise floor for frequencies between [20-40] kHz.

As temperature compensation was required for range measurements, a small form-factor PCB ($[2.5 \times 2.5]$ cm)(Figure 6.1(b)) was designed to mount the Sensirion SHT15 temperature /humidity sensor (along with a filter cap and necessary discrete components such as capacitors and pull-up resistors), and was controlled by the Fleck-3z microcontroller via a GPIO digital interface. It consumes < 5 mA of current, thus allowing it to be powered directly from the digital I/O ports of the mote.

Fleck-3z runs the TinyOS-2.x OS, and the software performs the tasks of maintaining and executing a schedule of system operations, maintaining a persistent log of system actions and status, sampling from attached on-board/external

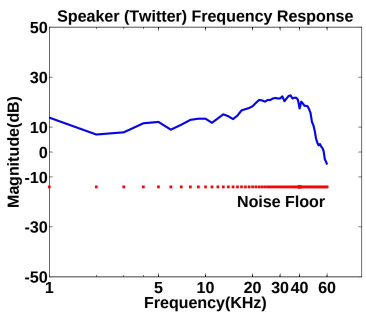

(a)

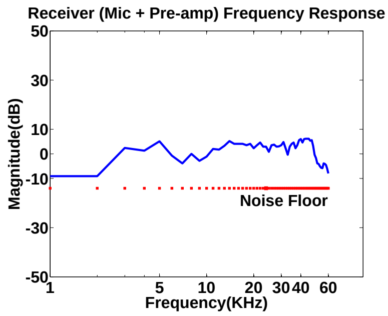

(b)

Figure 6.3: Mote-based system: Frequency response of the (a): Speaker and (b): Receiver front-end.

sensors, controlling the operation and power switch of the audio signal processing daughter board. The software for the Blackfin DSP is responsible for configuring (sampling rate, gain, etc) and enabling the audio codec ICs, managing the incoming and outgoing digital audio stream, transferring data/information to the micro-SD card, command exchange from the Fleck-3z via serial interface, such as start/stop audio playback/recording, interrogate operational status, etc.

6.2 Ranging Methodology

For this system, a [20-25] kHz/50 ms ranging signal was chosen, and the audio codes were configured to sample at 64 kHz. Although the audio codecs could support a maximum sampling rate of 192 kHz that can generate a signal upto 96 kHz, our system tests revealed that there was a significant drop in the audio output of approximately 30-40dB beyond 25 kHz frequency range. This limited our choice of the ultrasonic bandwidth to only 5 kHz.

The system uses the TDOA of RF and ultrasound signals to measure the beacon-to-listener distances. The beacon periodically transmits a RF message containing the measured ambient temperature and humidity. At the start of each RF message, each beacon transmits a broadband ultrasonic linear chirp pulse. The fast propagating RF signal leads its synchronous ultrasound pulse, and reaches the listener almost instantaneously, which then measures the TDOA between them. The TOA of the ultrasound pulse is measured by cross-correlating the received chirp pulse with a copy of the reference signal stored in the receiver, and then, estimates the range by the envelope detection technique (Section 4.1). Since the speed of sound has a relatively large sensitivity to temperature variations than relative humidity and atmospheric pressure, the final distance estimate is computed by the corresponding speed of sound obtained by averaging the ambient temperature measured at the beacon (sent in the RF message) and the listener (measured at the TOA of the ultrasound pulse). After carefully estimating the various system induced time-delays, a final calibration was performed to eliminate a random lag of 6.42 cm and was subtracted from the final result.

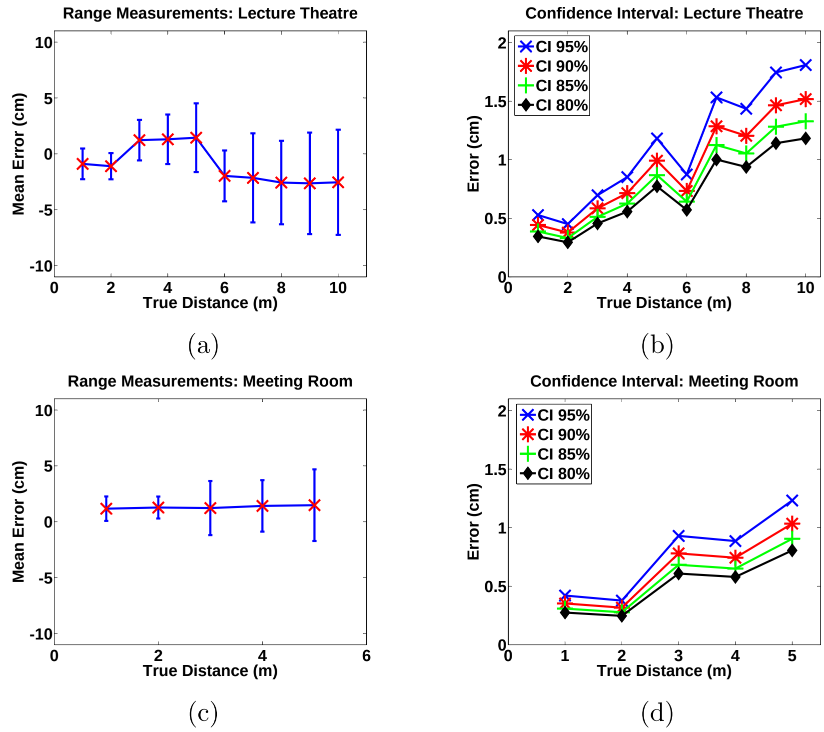

Figure 7.1: Accuracy in terms of mean error and deviation (shown in blue vertical lines), and Confidence Intervals for the different cases.

7 Experiments and Results

To evaluate the performance of our system under different multipath conditions, we conducted ranging experiments in the following environments:

Case-A - Indoor, Low multipath: A quiet lecture theatre ($[25 \times 15 \times 10]$ m) with a spacious podium at one end of the large room.
Case-B - Indoor, High mutipath: A quiet meeting room ($[7 \times 6 \times 6]$ m) with a big wooden table in the center and other office furnitures.
Case-C - Outdoor, Very low multipath: A less frequently used urban walkway, and the weather being sunny with mild breeze.

In all our experiments, the beacon mote was fixed while we performed a controlled and careful movement of the listener mote along the direct LOS using a measuring tape and markers for establishing the correct ground distance. The beacon was calibrated to chirp at 70 dB. The speed of sound used in distance calculation was according to the model: $c_{air} = 331.3 + 0.6\theta$ (θ: air temperature in ^{o}C). For every setting (i.e., different distances under different test cases), the experiments were repeated 30 times. The metrics used to evaluate the system were accuracy (difference between the ranging results and the true distance) and confidence interval for the measured errors.

The accuracy and confidence measurements for the case-A setting are shown in Figure 7.1-(a)&(b), where we can see that our system yields accurate and sta-

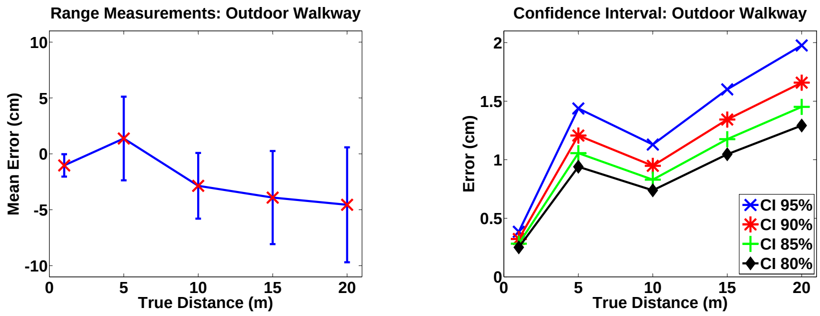

(a) (b)

Figure 7.2: Accuracy in terms of mean error and deviation (shown in blue vertical lines), and Confidence Intervals for the different cases.

ble ranging results in a (less severe) multipath environment. The mean ranging error is within $\pm$[1-2] cm with a 95% confidence interval of < 2 cm. High percentage of experiments recorded less than 2 cm accuracy, however, the performance deteriorates for distance measurements at [9-10] m when the listener mote approaches close to the walls. Even then, the error deviation from the mean is < 5 cm.

Figure 7.1-(c) shows the accuracy for case-B, where the mean ranging error is 1.5 cm and the maximum deviation is 2.5 cm at its maximum measured distance of 5 m. Due to the highly cluttered and multipath dominated environment, the reported error levels (for each measurement) is quite fluctuating, even for shorter distances. Nevertheless, the system was able to record a confidence interval < 1.5 cm (Figure 7.1-(d)).

The ranging statistics for case-C has been shown in Figure 7.2-(a)&(b). The system shows similar performance as reported for indoor case-A/B for distances < 10 m with a maximum mean error and deviation of ≈ 2.5 cm and an estimated confidence interval of 2 cm. We also observe that the the ranging error increases and shows a larger dynamic range for distance measurements at 15 m and 20 m, which is primarily due to the a lower SNR of the received signal caused by attenuation and non-uniformities in the atmosphere caused by wind. The measurements at 5 m shows a sudden drop in accuracy and an increased deviation, which is due to a strong breeze at that instant, but the system quickly recovers and attains a stable mean error.

For all the measurements, we observe that the absolute distance estimation error increases with the increase in separation between the transmitter and the receiver. In practice, distance information is not known a priori, therefore we have shown the distribution of all ranging errors in the different test environments (Figure 7.3) so as to provide an overall system snapshot. From the figure, we can see that the overall performance of our system is accurate with a mean error of 1 cm and deviation of 3.63 cm with the best performance obtained in indoor spacious facilities.

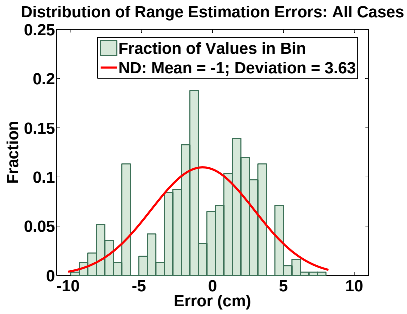

Figure 7.3: Overall System Performance.

8 Discussion

Our work has similarities to the linear chirp based system designed by Kushwaha [8]; but instead of using an additional Gaussian window to compensate for high correlation sidelobes, we use a simpler and effective envelope detection method. Our ranging precision (after temperature compensation) is generally 3× better, where for ranges between [10-20] m, our standard deviation is 5 cm compared to [15-25] cm reported by Kushwaha et al. Further, Kushwaha's system achieved a maximum detection range of 30 m at a SPL of 105 dB at 10 cm (i.e. measured at the near-field of the speaker). Such a near-field measurement may not provide the correct SPL representation, as they are dominated by the physical dimension of the speaker membrane and the volume of displaced air. In contrast, our system attained at maximum range of 30 m, but its operational range was 20 m at SPL of 70 dB (SPL measured at 1 m).

Our system reports, approximately, the same level of accuracy as the BeepBeep [10] system for ranges under 10 m. However, the authors do not provide any ranging analysis for distances over [10-12] m, which is where our system is more useful. There is no mention of the SPL for this system, therefore, comparing the ranges would be unfair.

The AENSBox system [9], calibrated to 105 dB SPL at 10 cm, attains a maximum range of 60 m with a mean error of 1.73 cm and deviation of 1.76 cm. It is 3× better than our system in maximum operational range, but the accuracy is comparable to ours with a mean of 1 cm and deviation of 3.63 cm. This additional benefit in range comes at the cost of using a longer (1/3 s) ranging signal and an expensive matched-filter. However, under the condition of duty-cycling (Figure 8.1-(a)), our system scores over AENSBox in consuming 80% lesser power. Table 8.1 compares the various resource usage between these two systems, where again, our system proves economical in saving power and processing cost.

A comparison of the signal envelope (that is an important factor for precision) among the mote-based system, AENSBox and BeepBeep has been shown in Figure 8.1-(b), where we consider the signal length of the various systems to be 1 s (for easy analysis). We observe that our system has a narrower signal envelope than the other compared systems, which implies that if the same SPL is generated from all, then our system would be able to attain comparable

Table 8.1: Resource Usage

System	**Power (W)**	**Approx. Processing Cost**
Mote-based System	2.5	2*FFT + 1*IFFT
AENSBox	3.6	5*FFT + 4*IFFT

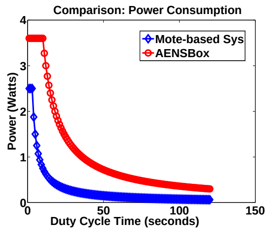

(a)

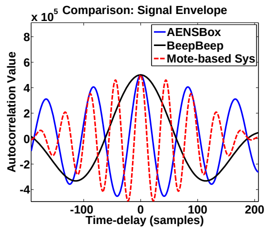

(b)

Figure 8.1: System Comparison.

detection range, but with better accuracy.

9 Future Work and Conclusion

The current limitation of the presented system is that its ranging accuracy degrades under dense multipath in cluttered environments, such as long and narrow office corridors, tunnels, small office rooms etc; and therefore, we are currently investigation robust algorithms that can improve system reliability under these extreme conditions. Our final objective is to develop an efficient localization and tracking system for indoor environments on mote-class devices.

To summarize, we presented a study of the impact of pulse length and bandwidth on range and resolution of broadband signals. Leveraging on this understanding, we evaluated the ranging performance of linear chirps, and proposed an easy and low-cost signal detection technique based on estimating the envelope of the correlated pulse using a simple least-square approximation approach to counter the effect of low-noise and multipath. Finally, we presented two ultrasonic broadband ranging systems using linear chirps for improved indoor/outdoor positioning.

Bibliography

[1] Yao Kung, R. E. Hudson, C. W. Reed, Chen Daching, and F. Lorenzelli. Blind beamforming on a randomly distributed sensor array system. *IEEE Journal on Selected Areas in Communications*, 16(8):1555–1567, 1998.

[2] A. Arora et. al. Exscal: elements of an extreme scale wireless sensor network. In *Embedded and Real-Time Computing Systems and Applications*, pages 102–108. IEEE, 2005.

[3] G Simon, M. Maroti, A. Ledeczi, G. Balogh, B. Kusy, and A. Nadas. Sensor network-based countersniper system. In *SenSys*, pages 1–12. ACM, 2004.

[4] H.B. Wang, C.E. Chen, Andreas M. Ali, Shadnaz Asgari, Ralph E. Hudson, K Yao, D. Estrin, and C. Taylor. Acoustic sensor networks for woodpecker localization. In *Conference on Advanced Signal Processing Algorithms, Architectures and Implementations*. SPIE, 2005.

[5] Geoff Werner-Allen, Konrad Lorincz, Jeff Johnson, Jonathan Lees, and Matt Welsh. Fidelity and yield in a volcano monitoring sensor network. In *OSDI*, pages 27–27. USENIX Association, 2006.

[6] Andreas Terzis, Annalingam Anandarajah, Kevin Moore, and I-Jeng Wang. Slip surface localization in wireless sensor networks for landslide prediction. In *IPSN*, pages 109–116. ACM, 2006.

[7] Wen Hu, Nirupama Bulusu, Chun Tung Chou, Sanjay Jha, Andrew Taylor, and Van Nghia Tran. Design and evaluation of a hybrid sensor network for cane toad monitoring. *ACM TOSN*, 5(1):1–28, 2009.

[8] M. Kushwaha, K. Molnar, J. Sallai, P. Volgyesi, M. Maroti, and A. Ledeczi. Sensor node localization using mobile acoustic beacons. In *MASS*, pages 9pp.–491. IEEE, 2005.

[9] Lewis Girod, Martin Lukac, Vlad Trifa, and Deborah Estrin. The design and implementation of a self-calibrating distributed acoustic sensing platform. In *SenSys*, pages 71–84. ACM, 2006.

[10] Peng Chunyi, Shen Guobin, Zhang Yongguang, Li Yanlin, and Tan Kun. Beepbeep: a high accuracy acoustic ranging system using cots mobile devices. In *SenSys*, pages 1–14. ACM, 2007.

[11] Jingbin Zhang, Ting Yan, John A. Stankovi, and Sang H. Son. Thunder: towards practical, zero cost acoustic localization for outdoor wireless sensor networks. *SIGMOBILE Mob. Comput. Commun. Rev.*, 11(1):15–28, 2007.

[12] Kwon YoungMin, K. Mechitov, S. Sundresh, Kim Wooyoung, and G. Agha. Resilient localization for sensor networks in outdoor environments. In *ICDCS*, pages 643–652. IEEE, 2005.

[13] Borriello Gaetano, Liu Alan, Offer Tony, Palistrant Christopher, and Sharp Richard. Walrus: wireless acoustic location with room-level resolution using ultrasound. In *MobiSys*, pages 191–203. ACM, 2005.

[14] Andy Harter, Andy Hopper, Pete Steggles, Andy Ward, and Paul Webster. The anatomy of a context-aware application. In *MOBICOM*, pages 59–68. ACM, 1999.

[15] Nissanka Bodhi Priyantha. *The Cricket Indoor Location System*. PhD thesis, Massachusetts Institute Of Technology, 2005.

[16] Andreas Savvides, Chih-Chieh Han, and Mani B. Strivastava. Dynamic fine-grained localization in ad-hoc networks of sensors. In *MobiCom*, pages 66–179. ACM, 2001.

[17] P. Misra, D. Ostry, and S. Jha. Improving the coverage range of ultrasound-based localization systems. In *WCNC*. IEEE, 2011.

[18] M. Hazas and A. Hopper. Broadband ultrasonic location systems for improved indoor positioning. *IEEE Transactions on Mobile Computing*, 5(5):536–547, 2006.

[19] Prasant Misra, Diet Ostry, Sanjay Jha, and Navinda Kottege. An envelope-detection based broadband ultrasonic ranging system for improved indoor/outdoor positioning. Technical Report UNSW-CSE-TR-1106, 2011.

[20] E. Charles Cook and Marvin Bernfeld. *Radar Signals: An introduction to theory and application.* Academic Press, 1967.

[21] `http://www.asus.com.au/product.aspx?P_ID=ZBWhAEnH6nDOBOOE`.

[22] `http://pdf.eicom.ru/datasheets/knowles_acoustics_pdfs/spm0204ud5/spm0204ud5.pdf`.